

GT2012-68253

## ABSOLUTE AND CONVECTIVE INSTABILITY IN GAS TURBINE FUEL INJECTORS

Matthew P. Juniper

Engineering Department  
University of Cambridge  
Trumpington Street, Cambridge,  
CB2 1PZ, United Kingdom  
Email: mpj1001@cam.ac.uk

### ABSTRACT

Hydrodynamic instabilities in gas turbine fuel injectors help to mix the fuel and air but can sometimes lock into acoustic oscillations and contribute to thermoacoustic instability. This paper describes a linear stability analysis that predicts the frequencies and strengths of hydrodynamic instabilities and identifies the regions of the flow that cause them. It distinguishes between convective instabilities, which grow in time but are convected away by the flow, and absolute instabilities, which grow in time without being convected away. Convectively unstable flows amplify external perturbations, while absolutely unstable flows also oscillate at intrinsic frequencies. As an input, this analysis requires velocity and density fields, either from a steady but unstable solution to the Navier–Stokes equations, or from time-averaged numerical simulations. In the former case, the analysis is a predictive tool. In the latter case, it is a diagnostic tool. This technique is applied to three flows: a swirling wake at  $Re = 400$ , a single stream swirling fuel injector at  $Re \sim 10^6$ , and a lean premixed gas turbine injector with five swirling streams at  $Re \sim 10^6$ .

Its application to the swirling wake demonstrates that this technique can correctly predict the frequency, growth rate and dominant wavemaker region of the flow. It also shows that the zone of absolute instability found from the spatio-temporal analysis is a good approximation to the wavemaker region, which is found by overlapping the direct and adjoint global modes. This approximation is used in the other two flows because it is difficult to calculate their adjoint global modes.

Its application to the single stream fuel injector demonstrates that it can identify the regions of the flow that are responsible for generating the hydrodynamic oscillations seen in LES and experimental data. The frequencies predicted by this technique are within a few percent of the measured frequencies. The technique also explains why these oscillations become weaker when a central jet is injected along the centreline. This is because the absolutely unstable region that causes the oscillations becomes convectively unstable.

Its application to the lean premixed gas turbine injector reveals that several regions of the flow are hydrodynamically unstable, each with a different frequency and a different strength. For example, it reveals that the central region of confined swirling flow is strongly absolutely unstable and sets up a precessing vortex core, which is likely to aid mixing throughout the injector. It also reveals that the region between the second and third streams is slightly absolutely unstable at a frequency that is likely to coincide with acoustic modes within the combustion chamber. This technique, coupled with knowledge of the acoustic modes in a combustion chamber, is likely to be a useful design tool for the passive control of mixing and combustion instability.

### NOMENCLATURE

- A 1<sup>st</sup> matrix in the generalized eigenvalue problem
- B 2<sup>nd</sup> matrix in the generalized eigenvalue problem
- D characteristic lengthscale

$f$	frequency (Hz)
$i$	$\sqrt{-1}$
$k$	axial wavenumber (complex)
$m$	azimuthal wavenumber (real integer)
$p$	pressure field
$\hat{p}$	pressure profile in radial direction
$\hat{q}$	state vector, $\hat{q} \equiv (\hat{\mathbf{u}}, \hat{p})^T$
$r$	radial coordinate
Re	Reynolds number
$s_1$	saddle point 1
$s_2$	saddle point 2
St	Strouhal number, $St \equiv fD/U$ (complex)
$St_i$	non-dimensional temporal growth rate
$St_r$	non-dimensional frequency
$t$	time
$U$	characteristic velocity
$u$	axial velocity
$\mathbf{u}$	velocity field, $\mathbf{u} \equiv (u, v, w)^T$
$\hat{\mathbf{u}}$	velocity profile in radial direction
$v$	radial velocity
$w$	azimuthal velocity
$x$	axial coordinate

#### Greek:

$\theta$	azimuthal coordinate
$\omega$	local angular frequency (complex)
$\omega_i$	local temporal growth rate
$\omega_r$	local angular frequency
$\omega_0$	local spatio-temporal angular frequency (complex)
$\omega_{0i}$	local spatio-temporal growth rate
$\omega_{0r}$	local spatio-temporal angular frequency
$\omega_g$	global angular frequency (complex)
$\omega_{gi}$	global growth rate
$\omega_{gr}$	global angular frequency

#### Superscripts:

$'$	direct perturbation
$+$	adjoint perturbation

#### Subscripts:

$g$	global
$i$	imaginary
$r$	real
$0$	spatio-temporal

## INTRODUCTION

In order to achieve high energy densities, the flows within the combustion chambers of rocket and gas turbine engines are turbulent. The turbulent kinetic energy is dissipated at small scales by the action of viscosity. It is provided at large scales by coherent structures, such as large scale vortices in the flow. These coherent structures entrain the fuel into the air so that they can mix at a molecular level and burn [1] [2]. They are observed across all ranges of Reynolds numbers [3] but are most easily recognised at lower Reynolds numbers, for example in the vortex shedding behind a cylinder. In experiments on gas turbine fuel injectors, these coherent structures have been found to strongly affect the entrainment of fuel and air [4] (pp240–241).

These large scale coherent structures are the nonlinear development of large scale linear instabilities. In shear layers, experiments show that the mixing rate is proportional to the growth rate of linear instabilities. This is shown by comparing the rate of scalar mixing in curved shear layers [5] with that in straight shear layers [6]. This works because, in a curved shear layer, the growth rate of linear instabilities depends on the direction of curvature relative to the velocity gradient. The growth rate of these linear instabilities, as well as their frequencies and mode shapes, can be predicted from a linear stability analysis of a steady base flow. In turbulent flows, the time averaged base flow is appropriate.

In the coaxial fuel injectors used in liquid oxygen/gaseous hydrogen rocket engines, the combustion efficiency increases when the exit of the oxygen tube is recessed inside the hydrogen tube [7]. This happens because a strong global instability is provoked by a region of strong absolute instability in the recessed region [8]. This provokes large scale spiralling and flapping structures that improve mixing between the oxygen and hydrogen [9]. Similarly, in coaxial gas turbine fuel injectors, large scale structures appear when the central tube is recessed inside the outer tube [10]. This is also due to absolute instability in the injector. In both cases, linear stability analysis provides physical insight that helps to explain why these injectors mix reactants particularly well.

Hydrodynamic oscillations are not the only large scale coherent structures in rocket and gas turbine combustors. There are also long wavelength acoustic waves. Sometimes these interact with hydrodynamic oscillations. Energy is fed into the acoustic waves due to the synchronisation of heat release and pressure oscillations. If the mechanical energy input exceeds the damping, the waves' amplitude increases, sometimes to dangerously high levels. Experiments in which fuel is injected into the shear layer behind a backwards-facing step in a long combustion chamber show that the amplitude of these acoustic waves becomes particularly high when the natural frequency of hydrodynamic oscillations behind the step is close to the natural frequency of acoustic waves in the chamber [11]. This is because the frequency of hydrodynamic oscillations, and hence the frequency of heat release

fluctuations, locks into the acoustic frequency when the acoustics reaches a sufficiently high amplitude [12]. In gas turbine fuel injectors, these hydrodynamic oscillations have been shown to lead to bursts of increased fuel air mixing [4], which provides a mechanism through which they can cause bursts of heat release.

Improving mixing and suppressing thermoacoustic oscillations provide two good motives to predict the frequencies and growth rates of hydrodynamic instabilities in fuel injectors. If the regions of the flow that cause the instabilities can be identified, one can see how they should be altered in order to enhance, suppress, or change the frequencies of the instabilities. The purpose of this paper is to describe an appropriate stability analysis and to present its application to three flows of increasing complexity: a swirling wake flow, a single stream swirling fuel injector, and a lean burn gas turbine fuel injector with five swirling streams.

## 1 ANALYSING HYDRODYNAMIC INSTABILITIES

Flows with hydrodynamic oscillations can be simulated with time-resolved computational methods such as DNS, LES and uRANS. DNS is prohibitively expensive above low Reynolds numbers and is therefore not useful for most practical situations. LES is expensive because the timescales of large scale structures are much larger than the timesteps required for numerical stability on grids that are sufficiently fine to resolve the small scales. uRANS is less expensive because only the large scale structures are resolved, although the turbulence models may not be adequate for many practical situations [13]. Although LES and uRANS can simulate flows that contain hydrodynamic instabilities and oscillations, they cannot identify the regions of the flow that are causing these oscillations and therefore give little physical insight into how they might be enhanced or suppressed.

Physical insight into the causes of these oscillations can be obtained by performing a linear stability analysis on the time-averaged flow and assuming that the nonlinear saturated behaviour is similar to that of the most unstable global mode. For simple flows, this is a reasonable assumption [14], and there is no reason to suspect that this is not the case for complex flows. Linear stability analyses reveal useful information, such as the core of the instability (the wavemaker region), the regions that are most sensitive to external forcing, and the regions that, if changed, have the most influence on the instability [15] [16].

A well known example of a global hydrodynamic instability is vortex shedding behind a cylinder. This arises due to a region of local absolute instability that exists immediately behind the cylinder [17]. (A region is absolutely unstable if it supports perturbations that grow in time but do not convect away.) This region of absolute instability is found with a local stability analysis. Numerical simulations show that this is the only region that is absolutely unstable [18] but, nevertheless, that it triggers a global mode that influences the entire flow.

Section 1.1 describes the local stability analysis used in this paper. It has been applied to several model problems that are relevant to fuel injection [8] [19] [20]. In the past, researchers have found it difficult to apply the local analysis to swirling flows and have had to resort to linear direct numerical simulation [21] [22]. The technique described here, however, can easily be applied to swirling flows. It can consider non-isothermal flow and compressible flow but the cases in this paper are all for isothermal flow.

### 1.1 Local stability analysis

There are three stages to the local analysis. The first stage is to calculate the local stability behaviour at each axial position. The second stage is to combine this behaviour to obtain the frequency of the global mode. The third stage is to force each axial position at the global mode frequency in order to evaluate the shape of the global mode.

The Navier-Stokes and mass conservations equation are linearized about a steady axisymmetric base flow. The base flow is assumed to be locally parallel and small local perturbations to the velocity,  $\mathbf{u}(x, r, \theta, t)$ , and pressure,  $p(x, r, \theta, t)$ , are assumed to have the form  $\hat{\mathbf{u}}(r)\exp(i(kx + m\theta - \omega t))$ . In this expression,  $k$  is the axial wavenumber,  $m$  is the azimuthal wavenumber, and  $\omega$  is the angular frequency of the corresponding perturbations. In general, the angular frequency is complex. Its real part is the angular frequency of the oscillations and its imaginary part is their growth rate. In this paper, each azimuthal wavenumber,  $m$ , is considered separately, so that  $m$  becomes a parameter in the problem, rather than a variable.

In order to satisfy the governing equations and boundary conditions, only certain combinations of  $k, m$ , and  $\omega$  are permitted. These are the eigenvalues of the system. These are found in practice by discretizing the governing equations and expressing them as a generalized matrix eigenvalue problem  $\mathbf{A}(k)\hat{q} = \omega\mathbf{B}(k)\hat{q}$ , where  $\mathbf{A}$  and  $\mathbf{B}$  are matrices and  $\hat{q}$  is the state vector  $(\hat{\mathbf{u}}, \hat{p})^T$ . For each value of  $k$ , there are as many values of  $\omega$  as there are discretization points. Some of these eigenvalues correspond to discrete modes (of the continuous system) and some correspond to the continuous spectrum. Only those corresponding to the discrete modes are considered here.

In the first stage of the local stability analysis, the maximum temporal growth rate,  $\omega$ , and the maximum spatio-temporal growth rate,  $\omega_0$ , are calculated. The maximum temporal growth rate is the eigenvalue with the highest value of  $\omega_i$  that can be obtained when  $k$  is a real number. It is found by calculating  $\omega$  over the range of real  $k$  for which  $\omega_i$  is positive and then iterating to the highest value of  $\omega_i$ . The maximum spatio-temporal growth rate is the eigenvalue with the highest value of  $\omega_i$  that can be obtained when  $d\omega/dk = 0$  (zero group velocity). This corresponds to the highest valid saddle point of  $\omega_i$  in the complex

$k$ -plane [23]. One hill of this saddle point is always connected to the maximum temporal growth rate, so this saddle point is found by starting from the maximum temporal growth rate and iterating  $k$  until  $d\omega/dk = 0$ .

If one considers how the flow responds to an impulse, the maximum temporal growth rate is the maximum growth rate of any wave in the corresponding wavepacket [24], while the spatio-temporal growth rate,  $\omega_{0i}$ , measures the growth rate of the perturbation with zero group velocity, which is the wave that stays at the point of impulse. The flow is locally absolutely unstable in the regions in which the spatio-temporal growth rate is positive. It is convectively unstable or stable elsewhere.

The second stage of the local analysis is to calculate the growth rate and frequency of the linear global mode. This global mode consists of two types of wave with zero group velocity: upstream waves, which decay to zero as  $x \rightarrow -\infty$ , and downstream waves, which decay to zero as  $x \rightarrow +\infty$ . These waves meet at a streamwise location,  $x_s$ , known as the wavemaker region. The easiest way to find  $x_s$  is to analytically continue  $\omega_0(x)$  into the complex  $x$ -plane and to locate the saddle point of  $\omega_0(x)$  (figure 7 of [23]). The value of  $\omega_0$  there is the growth rate of the global mode,  $\omega_g$ . In this paper, this saddle point is found by interpolating 8<sup>th</sup> order Padé polynomials through the known values of  $\omega_0$  and then extending these polynomials into the complex  $x$ -plane [25]. The frequency of the saturated nonlinear global mode is easier to find; it is the absolute frequency at the point where the flow transitions from convective instability to absolute instability [26].

The third stage of the local analysis is to evaluate the mode shape of the linear global mode by evaluating the response of each slice at the linear global mode frequency and then joining these mode shapes together [25]. The adjoint global mode is found in a similar way.

In this paper, the local stability behaviour is calculated with a software package called InstaFlow, which was created in 2009. Its application to gas turbine engines won the 2009 Environmental Technology award from the Engineer Magazine [27]. Together, the three stages take around one hour on a single processor.

## 2 RESULTS

The local analysis is presented for three flows: (i) the Rankine vortex with axial flow, (ii) a single stream swirling fuel injector that has already been extensively studied, and (iii) a lean burn fuel injector from a gas turbine engine.

### 2.1 The Rankine vortex with axial flow

The Rankine vortex has solid body rotation in its core and irrotational flow outside. The azimuthal velocity is continuous at the junction of the two regions and, in this case, the core and

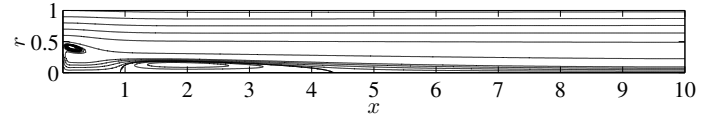


FIGURE 1. Streamlines of the Rankine vortex with axial flow.

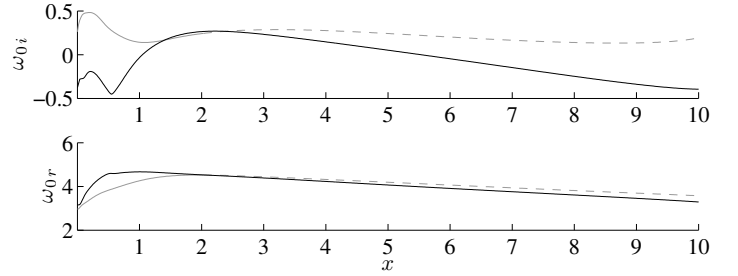


FIGURE 2. Spatio-temporal growth rate,  $\omega_{0i}$ , and spatio-temporal frequency  $\omega_{0r}$ , of saddle  $s_1$  (grey) and saddle  $s_2$  (black) of the  $m = 2$  mode for perturbations to the base flow in figure 1. The dashed line shows where the  $s_1$  saddle becomes invalid.

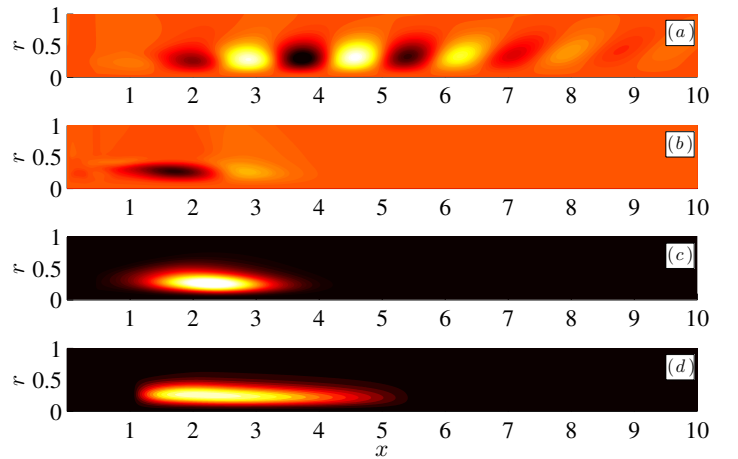


FIGURE 3. (a) Direct global mode,  $u'(x, r)$ , (b) adjoint global mode  $u^+(x, r)$ , (c) structural sensitivity [16], and (d) spatio-temporal eigenfunction for the  $m = 2$  perturbations from saddle  $s_2$  in figure 2. The colormaps span (a)  $[-1, 1]$ , (b)  $[-1, 1]$ , (c)  $[0, 1]$ , (d)  $[0, 0.27]$ .

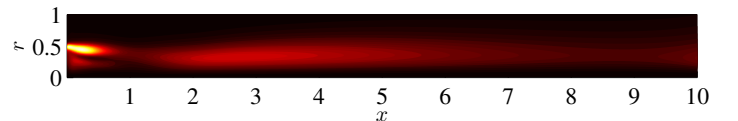


FIGURE 4. Spatio-temporal eigenfunction for  $m = 2$  perturbations from saddle  $s_1$  in figure 2. The colormap spans  $[0, 0.49]$ .

the exterior have different axial velocities. This velocity profile, with core radius of 0.5, is imposed at the inlet to a round domain, which extends to  $r = 4$  in the radial direction and  $x = 10$  in the axial direction. The Reynolds number is 400, defined in terms of the outer flow axial velocity,  $U$ , and the wake diameter,  $D$ . The swirl number is 0.7, defined as the azimuthal velocity divided by  $U$  at  $r = 0.5$ . The frequencies quoted here are non-dimensionalized by  $U/D$ . A steady solution (figure 1) to the nonlinear Navier–Stokes equations is found by imposing axisymmetry. This works because axisymmetric perturbations are stable. The flow evolves rapidly for  $0 < x < 0.5$  and slowly for  $x > 0.5$ . It has a short upstream recirculation bubble between  $0 < x < 0.4$  and a long downstream recirculation bubble between  $0.9 < x < 4.3$ . The fact that this flow has two recirculation bubbles makes it an interesting test case for the local stability analysis.

The first stage of the local analysis is to calculate the local stability behaviour. For this flow, the  $m = 2$  azimuthal mode is the most unstable and is the only one shown here. There are two influential saddle points, labelled  $s_1$  and  $s_2$ . Their spatio-temporal growth rates and spatio-temporal frequencies are shown in figure 2. Saddle  $s_1$  dominates for  $0 < x < 1.4$ , in the upstream bubble and becomes invalid for  $x > 2$ . Saddle  $s_2$  dominates for  $x > 1.4$  in the downstream bubble.

The second stage of the local analysis gives  $\omega_g = 3.47 + 0.298i$  for the upstream bubble ( $s_1$ ) and  $\omega_g = 4.51 + 0.231i$  for the downstream bubble ( $s_2$ ). The real component of  $\omega_g$  is the linear global mode's frequency, and the imaginary component is its amplitude. By comparison with figure 2, it can be seen that the frequency is approximately given by the value of  $\omega_{0i}$  where  $\omega_{0i}$  is a maximum. The value found with a bi-global analysis is  $\omega_g = 4.45 + 0.162i$ , which matches that of the downstream bubble. (In wake flows, local analyses over-predict the growth rate  $\omega_{gi}$  [16] [25]). This indicates that the downstream bubble ( $s_2$ ) dominates the global mode.

The shape of the linear global mode, found from the third stage of the local analysis, is shown in figure 3(a). This image shows streamwise velocity oscillations which, because  $m = 2$ , wind around the axis in a double helix pattern. The adjoint global mode is also calculated from the local analysis (figure 3b) [28]. When overlapped with the direct global mode (figure 3a), this gives the wavemaker region (figure 3c) [16]. This shows the region of the flow that is the core of the instability. In this case, the instability is driven by the strong axial and azimuthal shear in the recirculation bubble and is prevented from convecting away by the reverse flow there.

It is often convenient to present the results of the first stage of the analysis in a different way. Figure 3(d) shows the kinetic energy of the eigenfunction of saddle  $s_2$ ,  $E(r, x) \equiv (u^2(r, x) + v^2(r, x) + w^2(r, x))/2$ , multiplied by the local spatio-temporal growth rate,  $\omega_{0i}(x)$ . This quantity is called the spatio-temporal eigenfunction map. It shows the region of the flow that is re-

sponsible for the absolute instability. Unsurprisingly, it is very similar to the wavemaker region (figure 3c), which was found by overlapping the direct and adjoint global modes. While figure 3(d) shows this for saddle  $s_2$ , which is dominant, figure 4 shows this for saddle  $s_1$ , which is sub-dominant. This shows that the sub-dominant mode lies in the upstream bubble.

It is much easier and quicker to calculate the spatio-temporal eigenfunction map than it is to perform the second and third stages of the local analysis. Furthermore, the second and third stages can be inaccurate when applied to noisy data or to flows that are strongly non-parallel [29]. For these reasons, only the temporal and spatio-temporal eigenfunction maps are shown for the next flows.

For the nonlinear global mode, the frequency is determined by the absolute frequency at the point where the flow transitions from convective instability to absolute instability [26]. In this flow there are two such points. One is at the front of the upstream bubble and would cause a frequency of 3.1. The other is at the front of the downstream bubble and would cause a frequency of 4.6. The nonlinear frequency of this flow is not known but, if it were (e.g. from LES or experimental data), the dominant region of the nonlinear mode could be inferred. From the local analysis alone it is not possible to determine which will dominate. In swirling vortex breakdown bubbles, for instance, the dominant point switches from the upstream to the downstream recirculation bubble as the swirl increases [30].

## 2.2 Single stream swirling fuel injector

The second test case is a model fuel injector that is based on an industrial gas turbine injector. Previous experiments have shown that this design is susceptible to large thermoacoustic oscillations [31]. The hydrodynamic oscillations in this injector have been extensively studied under isothermal conditions, both experimentally [4] and numerically [13]. This section concerns the causes of these hydrodynamic oscillations.

The injector has a swirling outer stream with exit diameter  $D = 37.63$  mm and a central non-swirling jet with exit diameter 6.2 mm. The outer stream's bulk axial velocity is  $U = 1.99$  ms<sup>-1</sup>, its maximum axial velocity is 3.0 ms<sup>-1</sup>, and its maximum azimuthal velocity is 8.7 ms<sup>-1</sup>. The central jet's axial velocity is 5.3 ms<sup>-1</sup> and it can be switched off (figure 5a), or on (figure 6a). The amplitude of the hydrodynamic oscillations is found to be around 2 ms<sup>-1</sup> [13].

Dunham *et al.* [13] calculated the isothermal flow with LES and uRANS. They showed that LES gives a more faithful representation of the experimental results than uRANS. For example, the position of the swirl cone reattachment region is predicted more accurately. For this reason, LES, rather than uRANS, data is used for the local analysis in this paper. The natural frequency of hydrodynamic oscillations is already known from the LES and experimental data so the local analysis is used here to show

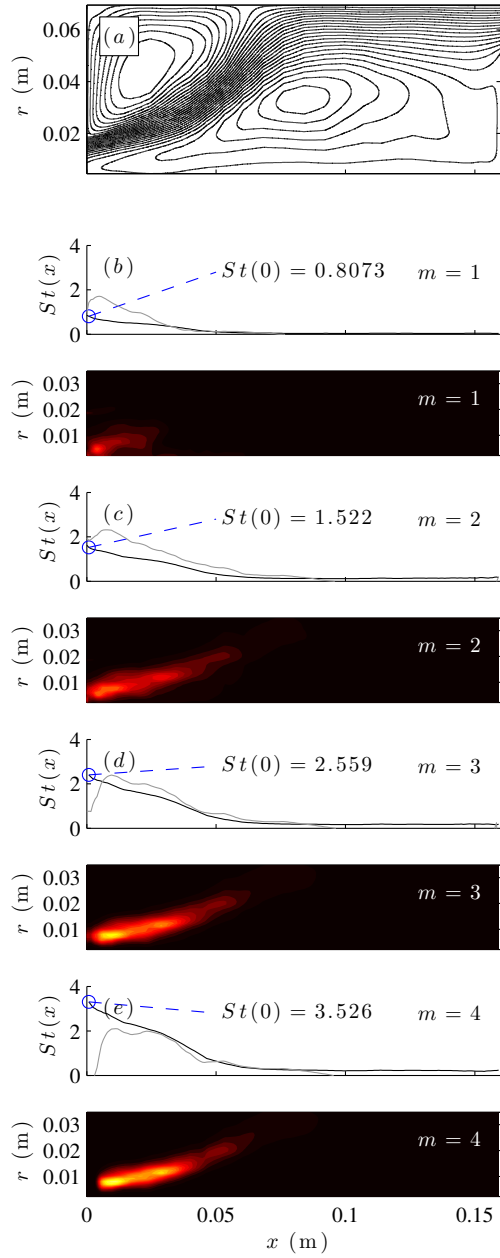


**FIGURE 5.** (a) Streamlines of the time-averaged LES velocity field for the single stream injector without a central jet, from Dunham *et al.* [13]. The flow enters on the left at  $0.01 < r < 0.0188$  and exits on the right at  $0.05 < r < 0.07$ . Frames (b)–(e) The spatio-temporal frequency,  $\omega_{0r}$ , spatio-temporal growth rate,  $\omega_{0i}$ , and the spatio-temporal eigenfunction maps for the azimuthal modes  $m = 1$  to  $m = 4$ . In (b)–(e) the spatio-temporal frequency,  $\omega_{0r}(x)$  (black lines), and the spatio-temporal growth rate,  $\omega_{0i}$  (grey lines, multiplied by 10), are expressed as Strouhal numbers, where  $St \equiv \omega D / (2\pi U)$  and  $D = 0.03763\text{m}$  and  $U = 1.99\text{ms}^{-1}$ ). The colormaps span  $[0, 5]$ .

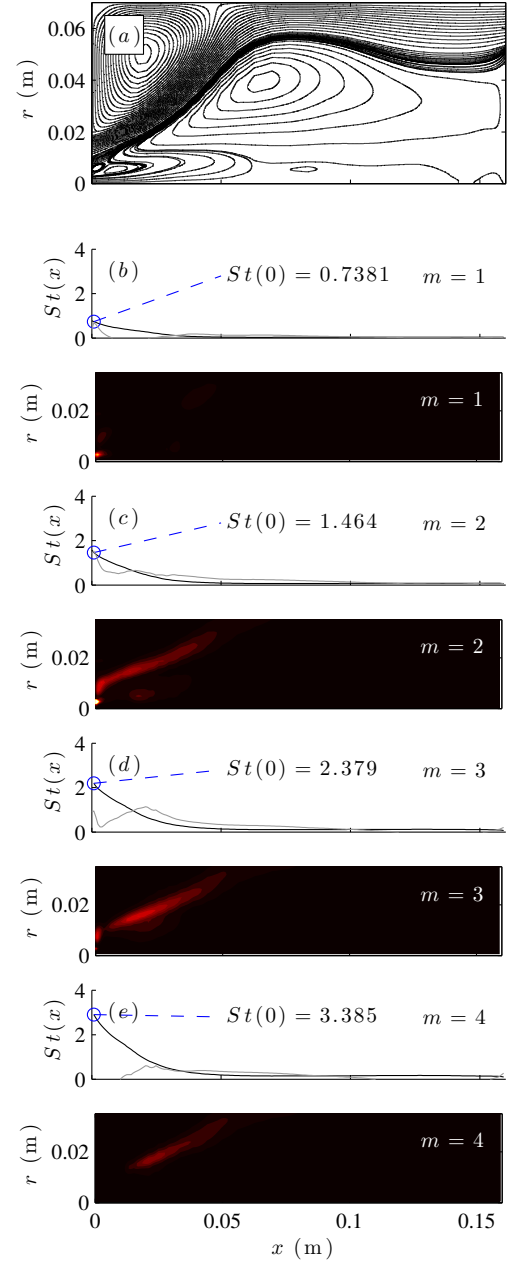


**FIGURE 6.** The same information as figure 5 but for the single stream injector with a central jet. In frame (a), the streamlines that start in the central jet have been shown with higher resolution. The colormaps spans  $[0, 5]$ .

where the core of the instability lies and how these instabilities can be inhibited.

Figure 5(b) shows that the  $m = 1$  mode of the no jet case has a positive spatio-temporal growth rate (grey line) for  $0 < x < 0.075$  m with a maximum at  $St_i = 0.17$ . (The growth rate is multiplied by 10 so that it can appear alongside the frequency.) The spatio-temporal frequency (black line) is  $St_r = 0.8073$  at entry and drops monotonically. The spatio-temporal eigenfunction map shows that the core of this instability lies in the upstream part of the shear layer between the swirling jet and the central recirculating zone. Stage 2 of the local analysis reveals that this mode has frequency  $St = 0.674$  (35.6 Hz). For comparison, the LES and experimental data of Dunham et al. [13] reveal a spectral peak at  $St = 0.67$  (35.4 Hz) in LES and  $St = 0.69$  (36.5 Hz) in experiments. The local analysis agrees well with both. The nonlinear global mode predicted by the local analysis, which is the absolute frequency of the most upstream point of absolute instability, has  $St = 0.8073$  (42.7 Hz). This is about 17% too high. It seems, therefore, that the nonlinear global mode frequency is best estimated from the linear global mode frequency or the absolute frequency at the point where the absolute growth rate is a maximum, which is  $St = 0.662$  (35.0 Hz) at  $x = 0.0046$  m.

Figure 5(c)–(e) show the same information for  $m = 2, 3$  and 4. For these modes, the core of the instability also lies in the shear layer between the swirling jet and the central recirculating zone but extends further downstream. The  $m = 2$  mode has the highest absolute growth rate but the eigenfunction of the  $m = 4$  mode is thinner, which is why it appears to have a higher amplitude in the image. It is worth noting that the  $m = 3$  and  $m = 4$  modes have a small, or negative, growth rate at entry.

Stage 2 of the local analysis gives  $St = 1.396$  (73.8 Hz) for  $m = 2$ ,  $St = 2.122$  (112.2 Hz) for  $m = 3$ , and  $St = 2.672$  (141.3) for  $m = 4$ . For comparison, the LES and experimental data of Dunham et al. [13] reveal a second spectral peak at  $St = 1.34$  (70.9 Hz) in LES and  $St = 1.39$  (73.5 Hz) in experiments, but no further spectral peaks. This data also reveals that the mode shape is a combination of the  $m = 1$  and  $m = 2$  modes. The spectral peaks in the LES and experimental data clearly correspond to the  $m = 1$  and  $m = 2$  modes calculated with the local analysis. The absence of the  $m = 3$  and  $m = 4$  modes in the LES and experimental data is probably explained by the fact that the  $m = 1$  and  $m = 2$  modes start growing further upstream than the  $m = 3$  and  $m = 4$  modes and therefore dominate in the nonlinear regime.

Figure 5 shows that the wavemaker regions of all the modes lie in the upstream region of the shear layer, between the swirling jet and the recirculating zone. As for the Rankine vortex in section 2.1, the axial and azimuthal shear drive the instability and the reverse flow prevents it from convecting away. This suggests that these instabilities could be weakened by blowing a jet of air axially into this region so that perturbations are convected more rapidly downstream, making the flow less absolutely unstable there. This is confirmed by the results for the case with a cen-

tral jet, which are shown in figure 6 on the same scale as figure 5. The spatio-temporal eigenfunction map shows that the wavemaker region of each mode remains in the shear layer between the swirling jet and the central recirculation zone, which has shifted radially outwards. The absolute growth rates, however, are significantly lower. The only area of reasonably strong absolute instability is the small double recirculation bubble between the swirling jet and the central jet, around  $(x, r) = (0, 0.004)$ , but this is unstable only for the  $m = 1$  and  $m = 2$  modes.

Stage 2 of the local analysis, applied to this region, predicts that the only unstable linear global mode is  $m = 2$  with  $St = 1.48$  (78.3 Hz). The  $m = 1$  mode is globally stable. For comparison, the LES and experimental data of Dunham et al. [13] reveal a spectral peak at  $St = 1.44$  (76.2 Hz) in LES and  $St = 1.39$  (73.5 Hz) in experiments, whose mode shape is the  $m = 2$  mode. There is also a very weak second peak at  $St = 2.88$  (152.2 Hz) in LES and  $St = 2.78$  (147.0 Hz) in experiments. This does not correspond to the  $m = 3$  or  $m = 4$  modes so is likely to be the first harmonic of the  $m = 2$  mode.

In summary, a local analysis of the time-averaged LES data predicts global mode frequencies and shapes that agree well with the time-resolved LES and experimental results. In addition to this, the local analysis reveals the wavemaker regions of the corresponding global modes and explains why these global modes are weakened by the addition of a central jet.

### 2.3 Lean burn fuel injector

The third example is a generic lean burn fuel injector, which has five coaxial swirling air streams. Liquid fuel is injected between the first and second stream, to create a pilot flame, and between the fourth and fifth stream, to create the main flame. Here, the hydrodynamic stability of the injector is studied without fuel injection. The base flow is taken from time-averaged LES data. All quantities are non-dimensionalized with respect to the diameter,  $D$ , and the maximum axial velocity,  $U$ , of the central stream.

Five of the unstable modes of this flow are shown in figure 7: one along the axis of the injector, three at the interfaces between the streams, and one at the interface between the outer stream and the gas in the chamber. They are all for the  $m = 1$  mode, which is the most unstable.

The graphs in figure 7(a–e) show the temporal frequency (grey) and the spatio-temporal frequency (black) as a function of downstream distance,  $St(x)$ . The images in figure 7(a–e) show two different eigenfunction maps. The top half of each image shows the temporal eigenfunction multiplied by the temporal growth rate, while the bottom half shows the spatio-temporal eigenfunction multiplied by the spatio-temporal growth rate, as in figures 5 and 6. In general terms, the top half shows how unstable the mode is, while the bottom half shows how self-sustained it is.

Figure 7(a) shows the mode along the centreline. This mode is unstable and self-sustained, at  $St \approx 2$ . It corresponds to a helical motion that rotates (in time) in the same direction as the swirl but winds (in space) in the opposite direction. It is the cause of the precessing vortex core often seen in this type of injector. This generates large scale coherent structures that are likely to aid mixing throughout the injector. This instability is driven by the axial shear and is held in place by the low velocity region along the centreline of this confined swirling flow. It could be removed by injecting a jet along the centreline, as for the single stream injector, although this is unlikely to be desirable.

Figure 7(b) shows the mode between the first and second streams. This mode is convectively unstable, at  $St \approx 10$ , but is not self-sustained. This mode is caused by azimuthal shear between these two streams but exists in a region of high axial flow. This means that perturbations here are quickly convected downstream by the flow and are therefore not absolutely unstable.

Figure 7(c) shows the mode between the second and third streams, which is also driven by axial and azimuthal shear. This mode is unstable and weakly self-sustained, which means that it oscillates naturally at  $St \approx 0.5$  and responds strongly to forcing around that frequency. If liquid fuel were to be injected here, it is likely that heat release fluctuations would occur at this frequency. The frequency of this hydrodynamic mode is close to the frequencies of typical thermoacoustic modes in the combustion chamber and, depending on the overlap of the mode shapes, it is possible that the two types of mode will lock into each other, as seen in [11].

Figures 7(d–e) show the modes in the outer streams. They are unstable at  $St \approx 0.1$  and  $St \approx 0.3$ , but very weakly self-sustained.

This analysis quickly reveals the mode shapes of hydrodynamic instabilities, their frequencies, the degree to which they are self-sustained and their wavemaker regions. It can be applied to any fuel injector and provides useful guidance for design engineers. For example, this analysis shows that the precessing vortex core at  $St \approx 2$  is caused by the region of confined swirling flow along the centreline. It suggests that removing this confined region, or injecting flow along the centreline, is likely to eliminate this mode. Secondly, this analysis shows that small high frequency structures will develop between the first and second streams but be swept quickly downstream. It is not yet clear how useful these structures can be for driving fuel/air mixing. On the positive side, their frequencies are too far from typical thermoacoustic frequencies for the hydrodynamic oscillations to lock into the thermoacoustic oscillations. On the negative side, their corresponding wavelengths and saturation amplitudes are small so they will not create very large scale structures to drive entrainment and mixing. Their usefulness will have to be determined by analysing more fuel injectors and comparing their overall performance with the results of the analysis presented in this paper. Thirdly, this analysis shows that the flow between the

second and third streams has a resonant frequency that is close to thermoacoustic modes in the combustion chamber. If the shape of the corresponding hydrodynamic mode overlaps with that of the thermoacoustic mode, this could cause strong thermoacoustic oscillations.

### 3 CONCLUSIONS

Hydrodynamic instabilities in gas turbine fuel injectors generate large scale coherent structures. These aid mixing but can sometimes lock into acoustic modes in the combustion chamber, making a combustion system more susceptible to thermoacoustic oscillations. This paper describes a technique that can predict the frequencies of hydrodynamic instabilities and identify the regions of the flow that causes them.

First, this technique is applied to a swirling wake at  $Re = 400$ . This is a steady but unstable flow in which there are two recirculation bubbles. The technique shows that each bubble causes a hydrodynamic instability and that the instability of the larger bubble dominates. The results from this technique compare well with a linear global analysis. For this flow, the wavemaker region is identified by overlapping the direct and adjoint eigenfunctions (figure 3c). It is shown that a similar result can be obtained by multiplying the spatio-temporal eigenfunction by the spatio-temporal growth rate, which is easier and less error-prone (figure 3d).

Second, this technique is applied to a single stream swirling fuel injector at  $Re \sim 10^6$ . This approach differs from the first because the base flow is taken from time-averaged LES data, rather than from a steady but unstable solution to the Navier–Stokes equations. In this case, the technique is used as a diagnostic tool rather than a predictive tool. The technique identifies the wavemaker regions for the first four azimuthal modes ( $m = 1, 2, 3, 4$ ), which all happen to lie in the same place. The calculated global frequencies of the  $m = 1$  and  $m = 2$  modes are within a few percent of those measured from the time-resolved LES data. In this case, the nonlinear frequency selection criterion of Pier [26] does not seem to work as well as the conventional linear frequency selection criterion [23]. It seems therefore that the  $m = 1$  and  $m = 2$  modes are active but the  $m = 3$  and  $m = 4$  are not, which is likely to be because the  $m = 1$  and  $m = 2$  modes have higher upstream growth rates than the  $m = 3$  and  $m = 4$  modes, a feature also revealed by this technique. The technique explains how the addition of a central jet to this flow weakens its hydrodynamic instability. This is because the jet blows away the region of absolute instability between the swirling jet and the recirculation zone.

Third, this technique is applied to a lean burn gas turbine fuel injector, which contains five swirling streams. The technique identifies several different wavemaker regions, each corresponding to a different instability of the  $m = 1$  mode. Each wavemaker region has its own range of natural frequencies and



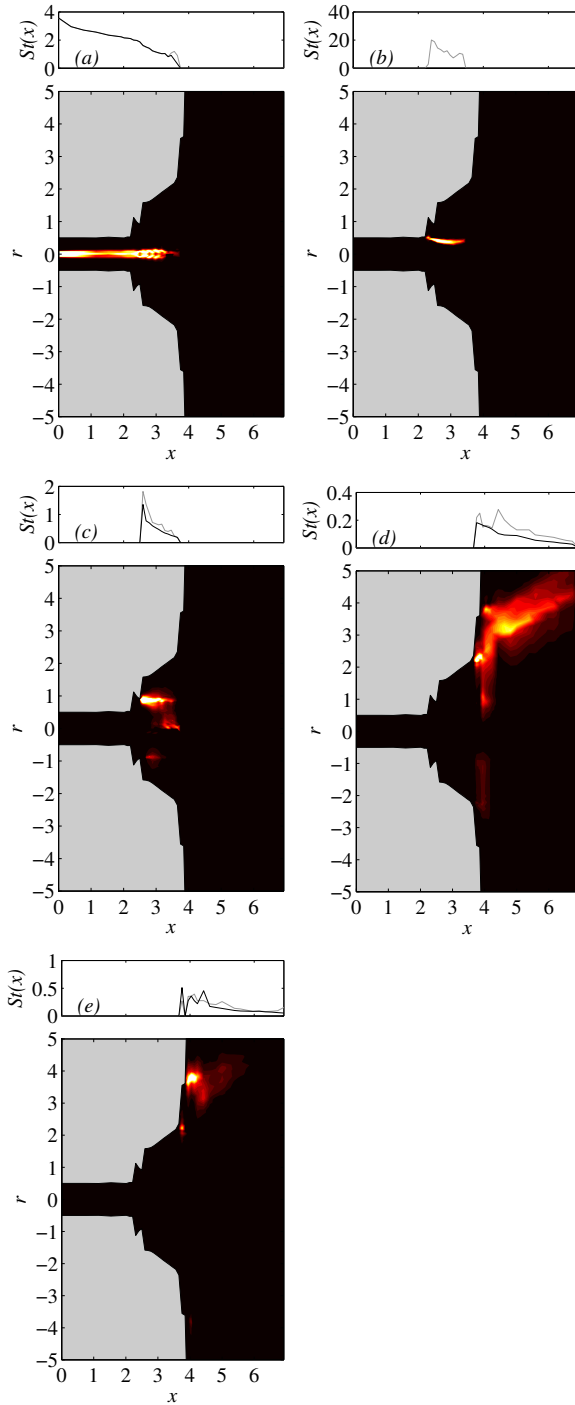


**FIGURE 7.** The five most unstable modes in the lean burn fuel injector. For each mode (a–e), the graphs show the temporal frequency,  $\omega_r$  (grey line), and the spatio-temporal frequency,  $\omega_{0r}$  (black line). The images show the temporal eigenfunction multiplied by the temporal growth rate (top half) and the spatio-temporal eigenfunction multiplied by the spatio-temporal growth rate (bottom half).

different stability characteristics. For example, the central region is strongly absolutely unstable and sets up a precessing vortex core at  $St \approx 2$ ; the region between the first two streams is strongly convectively unstable and tends to amplify maximally at  $St \approx 10$ ; and the region between the second and third streams is weakly absolutely unstable and oscillates at  $St \approx 0.5$ , which would typically be close to an acoustic frequency in the combustion chamber.

By identifying the hydrodynamic instabilities in a fuel injector and then comparing their frequencies and mode shapes with those of acoustic modes in the combustion chamber, it will be possible to identify which hydrodynamic instabilities are responsible for mixing and which could be contributing to thermoacoustic instabilities. This will be a useful design tool for the passive control of mixing and thermoacoustic instability.

## ACKNOWLEDGMENT

I would like to thank David Dunham and Adrian Spencer of Loughborough University for providing the time-averaged LES data from their paper [13], and Ubaid Qadri for calculating the base flow and linear global modes for the Rankine vortex with axial flow.

## REFERENCES

- [1] Broadwell, J. E. & Breidenthal, R. E., 1982, “A simple model of mixing and chemical reaction in a turbulent shear layer”, *J. Fluid Mech.* **125**, 397–410.
- [2] Aref & Jones, 1989, “The fluid mechanics of stirring and mixing”, *Phys. Fluids A* **1**, 470.
- [3] Broadwell, J. E. & Mungal, M. G., 1991, Large-scale structures and molecular mixing, *Phys. Fluids A* **3** (5), 1193.
- [4] Midgley, K., 2005, “An isothermal experimental study of the unsteady fluid mechanics of gas turbine fuel injector flowfields”, Ph.D. thesis, Loughborough University, U.K.
- [5] Karasson, P. S. & Mungal, M. G., 1996, “Scalar mixing and reaction in plane liquid shear layers”, *J. Fluid Mech.* **323**, 23–63.
- [6] Karasson, P. S. & Mungal, M. G., 1997, “Mixing and reaction in curved liquid shear layers”, *J. Fluid Mech.* **334**, 381–409.
- [7] Gill, G., 1978, “A qualitative technique for concentric tube element optimization, utilizing the factor (dynamic head ratio-1)”, AIAA Paper 7876.
- [8] Juniper, M., 2008, “The effect of confinement on the stability of non-swirling round jet/wake flows”, *J. Fluid Mech.* **605**, 227–252.
- [9] Juniper, M. & Candel, S., 2003, “The stability of ducted compound flows and consequences for the geometry of coaxial injectors”, *J. Fluid Mech.* **482**, 257–269.

- [10] Garcia-Villalba, Frohlich & Rodi, 2006, "Numerical simulations of isothermal flow in a swirl burner", ASME Turbo Expo GT2006-90764.
- [11] Chakravarthy S., Shreenivasan, O., Boehm, B., Dreizler, A. & Janicka, J., 2007, "Experimental characterization of onset of acoustic instability in a nonpremixed half-dump combustor", J. Acoust. Soc. Am.. **122** (1), 120
- [12] Juniper M., Li, L. & Nichols, J., 2008, "Forcing of self-excited round jet diffusion flames", Proc. Comb. Inst. **32** (1), 1191–1198.
- [13] Dunham, D., Spencer, A., McGuirk, J., Dianat, M., 2008, "Comparison of uRANS and LES CFD Methodologies for air swirl fuel injectors", ASME Turbo Expo GT2008-50278.
- [14] Barkley, D., 2006, "Linear analysis of the cylinder wake mean flow", Europhys. Lett. **75** (5) 750-756.
- [15] Hill, D., 1992, "A theoretical approach for analyzing the re-stabilization of wakes", AIAA Paper 92-0067
- [16] Giannetti, F. & Luchini, P., 2007, "Structural sensitivity of the first instability of the cylinder wake", J. Fluid Mech. **581**, 167–197.
- [17] Koch, W., 1985, "Local instability characteristics and frequency determination of self-excited wake flows", J. Sound Vib. **99**, 53–83.
- [18] Hannemann, K. & Oertel, H., 1989, "Numerical simulation of the absolutely and convectively unstable wake", J. Fluid Mech. **199**, 55–88.
- [19] Rees, S. & Juniper, M., 2009, "The effect of surface tension on the stability of unconfined and confined planar jets and wakes", J. Fluid Mech. **633**, 71–97.
- [20] Rees, S. & Juniper, M., 2010, "The effect of confinement on the stability of viscous planar jets and wakes", J. Fluid Mech. **656**, 309–336.
- [21] Delbende, I., Chomaz, J-M & Huerre, P., 1998, "Absolute/convective instabilities in the Batchelor vortex: a numerical study of the linear impulse response", J. Fluid Mech. **355**, 229–254.
- [22] Gallaire, F., Ruith, M., Meiburg, E., Chomaz, J-M & Huerre, P., 2006, "Spiral vortex breakdown as a global mode", J. Fluid Mech. **549**, 71–80.
- [23] Huerre, P. & Monkewitz, P., 1990, "Local and global instabilities in spatially developing flows", Ann. Rev. Fluid Mech. **22**, 473–537.
- [24] Juniper, M., 2007, "The full impulse response of two-dimensional jet/wake flows and implications for confinement", J. Fluid Mech. **590**, 163–185.
- [25] Juniper, M., Tammisola, O. & Lundell, F., 2011, "The local and global stability of confined planar wakes at intermediate Reynolds number", J. Fluid Mech. **686**, 218–238.
- [26] Pier, B., Huerre, P. & Chomaz, J-M, 2001, "Bifurcation to fully nonlinear synchronized structures in slowly varying media", Physica D **148**, 49–96.
- [27] Nathan, S., 2009, "Clean Engines on the front burner", The Engineer Magazine Awards 2009 Supplement 14–16.
- [28] Juniper, M. & Pier, B., 2010, "Structural sensitivity calculated with a local stability analysis", Eur. Fluid Mech. Conf., Bad Reichenhall, Germany, Sept. 2010
- [29] Mistry, D., Qadri, U. & Juniper, M., 2012, "Local stability analysis of a vortex breakdown bubble", J. Fluid Mech. (in preparation)
- [30] Qadri, U., Mistry, D. & Juniper, M., 2012, "Sensitivity analysis of spiral vortex breakdown", J. Fluid Mech. (submitted)
- [31] Lartigue, G., Meier, U. & Berat, C., 2004, "Experimental and numerical investigation of self-excited combustion oscillations in a scaled gas turbine combustor", Appl. Thermal Eng. **24** (11) 1583–1592.